

## SUPPORTING INFORMATION

### Multifunctional One-Dimensional Rhodium(I)–Semiquinonato Complex: Substituent Effects on Crystal Structures and Solid-State Properties

Minoru Mitsumi,<sup>†,‡,\*</sup> Shoji Ohtake,<sup>†</sup> Yuki Kakuno,<sup>†</sup> Yuuki Komatsu,<sup>†</sup> Yoshiki Ozawa,<sup>†,‡</sup>  
Koshiro Toriumi,<sup>†,‡</sup> Nobuhiro Yasuda,<sup>§</sup> Nobuaki Azuma,<sup>||</sup> and Yuji Miyazaki<sup>||</sup>

<sup>†</sup> Department of Material Science, <sup>‡</sup> Research Center for New Functional Materials,  
Graduate School of Material Science, University of Hyogo,  
3-2-1 Kouto, Kamigori-cho, Ako-gun, Hyogo 678-1297, Japan

<sup>§</sup> Japan Synchrotron Radiation Research Institute/SPring-8,  
1-1-1 Kouto, Sayo-cho, Sayo-gun, Hyogo 679-5198, Japan

<sup>||</sup> Research Center for Structural Thermodynamics, Graduate School of Science, Osaka University,  
1-1 Machikaneyama, Toyonaka, Osaka 560-0043, Japan

\*E-mail: mitsumi@sci.u-hyogo.ac.jp

**Table S1.** Selected Bond Lengths (Å) for [Rh(3,6-DBSQ-4,5-PDO)(CO)<sub>2</sub>]<sub>∞</sub> (**4**) and [Rh(3,6-DBSQ-4,5-(*N,N'*-DEN))(CO)<sub>2</sub>]<sub>∞</sub> (**5**)

|          | <b>4</b> at 240 K | <b>4</b> at 180 K |          | <b>5</b> at 250 K |
|----------|-------------------|-------------------|----------|-------------------|
| Rh1–Rh2  | 3.0943(6)         | 3.0108(6)         | Rh1–Rh2  | 2.9662(8)         |
| Rh1–Rh2* | 3.0313(6)         | 3.0115(6)         | Rh1–Rh2' | 3.2266(8)         |
| Rh1–O1   | 2.0125(16)        | 2.0193(19)        | Rh1–O1   | 1.995(4)          |
| Rh1–O2   | 2.0114(17)        | 2.017(2)          | Rh1–O2   | 2.007(4)          |
| Rh1–C18  | 1.857(3)          | 1.865(3)          | Rh1–C22  | 1.863(7)          |
| Rh1–C19  | 1.861(3)          | 1.867(3)          | Rh1–C23  | 1.850(6)          |
| Rh2–O7   | 2.0124(17)        | 2.017(2)          | Rh2–O5   | 2.000(4)          |
| Rh2–O8   | 2.0102(17)        | 2.012(2)          | Rh2–O6   | 1.995(4)          |
| Rh2–C37  | 1.860(3)          | 1.861(3)          | Rh2–C45  | 1.854(7)          |
| Rh2–C38  | 1.855(3)          | 1.862(3)          | Rh2–C46  | 1.857(7)          |

\* Symmetry operation:  $x + 1, y, z$ . ' Symmetry operation:  $x - 1, y, z$ .

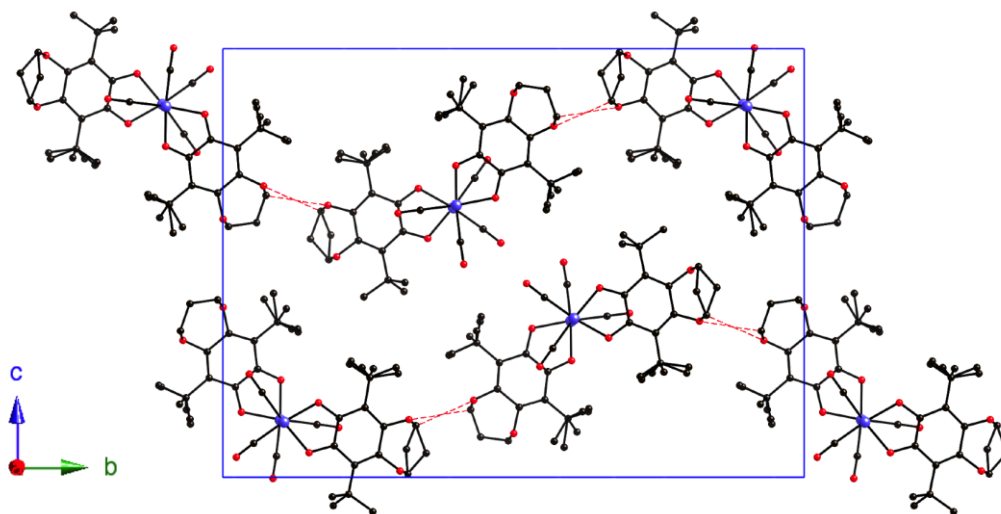


**Figure S1.** Crystal structure of  $[\text{Rh}(3,6\text{-DBSQ-4,5-PDO})(\text{CO})_2]_\infty$  (**4**) at 240 K in the RT phase viewed from  $a$ -axis. Interchain  $\text{C-H}\cdots\text{O}$  hydrogen bonds are drawn as red dashed lines;  $\text{O3}\cdots\text{C34} = 3.570(6)$  Å and  $\text{O9}\cdots\text{C15} = 3.603(5)$  Å.

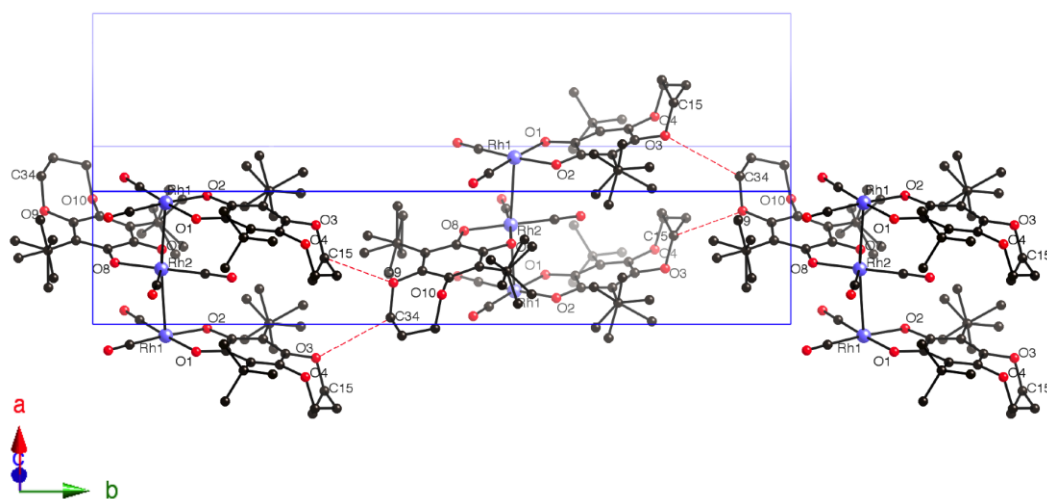


**Figure S2.** Crystal structure of  $[\text{Rh}(3,6\text{-DBSQ-4,5-PDO})(\text{CO})_2]_\infty$  (**4**) at 240 K in the RT phase showing the interchain  $\text{C-H}\cdots\text{O}$  hydrogen bonds between adjacent 1D chains;  $\text{O3}\cdots\text{C34} = 3.570(6)$  Å and  $\text{O9}\cdots\text{C15} = 3.603(5)$  Å.

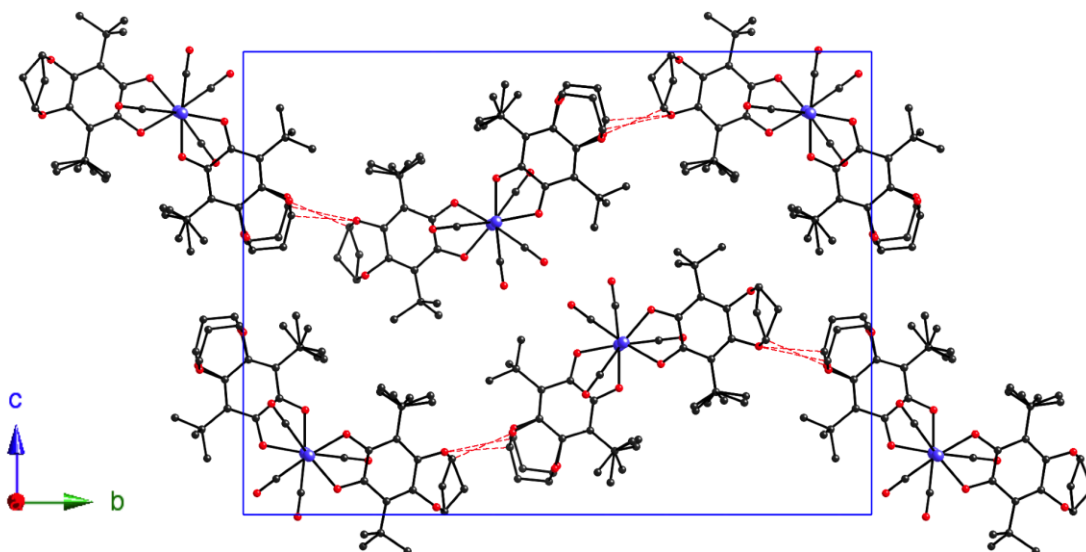


**Figure S3.** Crystal structure of  $[\text{Rh}(3,6\text{-DBSQ-4,5-PDO})(\text{CO})_2]_\infty$  (**4**) at 180 K in the LT phase viewed from *a*-axis. Interchain C–H $\cdots$ O hydrogen bonds are drawn as red dashed lines; O3 $\cdots$ C34A = 3.450(12) Å, O3 $\cdots$ C34B = 3.555(14) Å, and O9B $\cdots$ C15 = 3.433(10) Å.

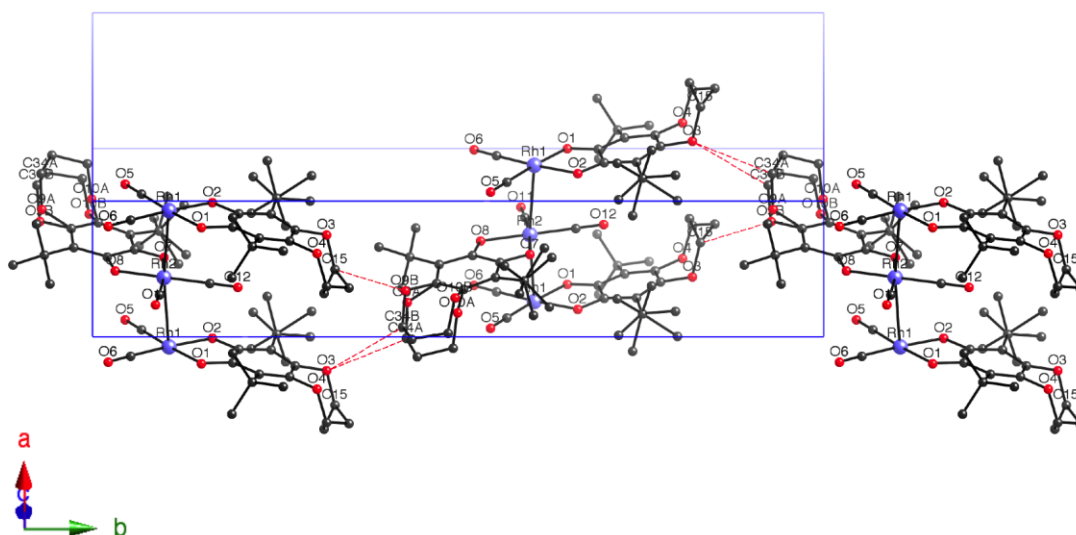


**Figure S4.** Crystal structure of  $[\text{Rh}(3,6\text{-DBSQ-4,5-PDO})(\text{CO})_2]_\infty$  (**4**) at 180 K in the LT phase showing the interchain C–H $\cdots$ O hydrogen bonds between adjacent 1D chains; O3 $\cdots$ C34A = 3.450(12) Å, O3 $\cdots$ C34B = 3.555(14) Å, and O9B $\cdots$ C15 = 3.433(10) Å.

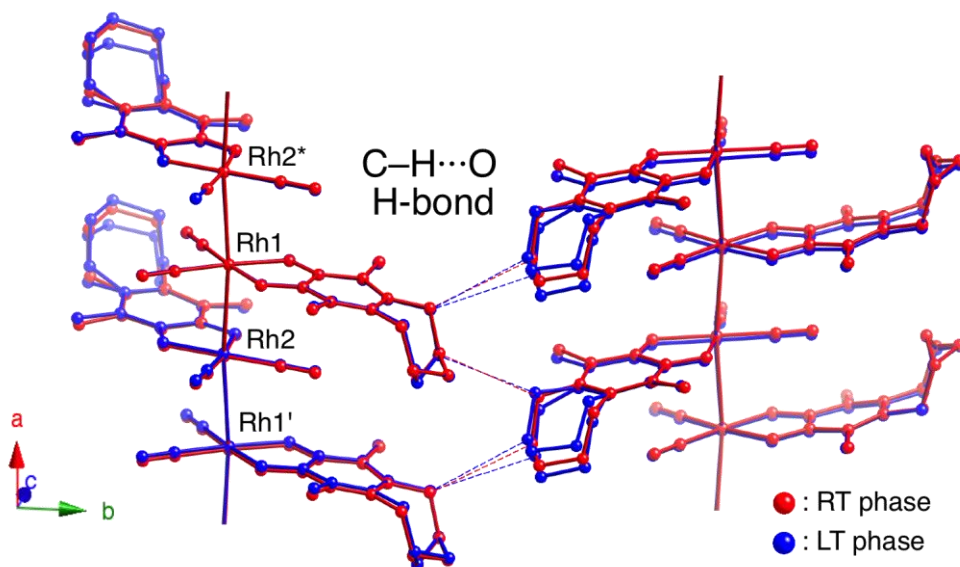


**Figure S5.** Superimposed drawing of the 1D chains of  $[\text{Rh}(\text{3,6-DBSQ-4,5-PDO})(\text{CO})_2]_\infty$  (**4**) in the RT (240 K) and LT (180 K) phases shown as red (RT phase) and blue (LT phase) ball-and-stick models by the overlapping of both of the Rh1 atoms. Dotted lines represent the intermolecular C-H...O hydrogen bonds between the adjacent 1,3-propanedioxy moieties; the methyl carbon atoms of *t*-Bu groups are omitted for clarity.

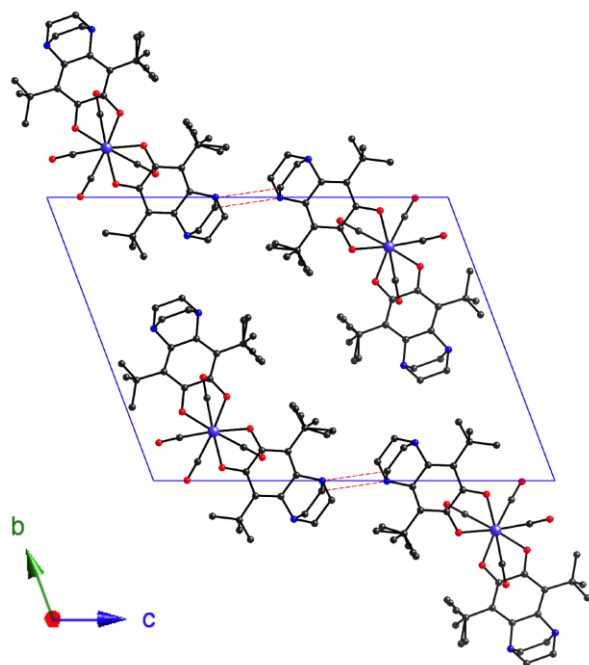


**Figure S6.** Crystal structure of  $[\text{Rh}(3,6\text{-DBSQ-4,5-(}N,N'\text{-DEN))}(\text{CO})_2]_\infty$  (**5**) at 250 K viewed from  $a$ -axis. Interchain  $\text{C-H}\cdots\text{N}$  hydrogen bonds are drawn as red dashed lines;  $\text{N4}\cdots\text{C42} = 3.553(8) \text{ \AA}$ .

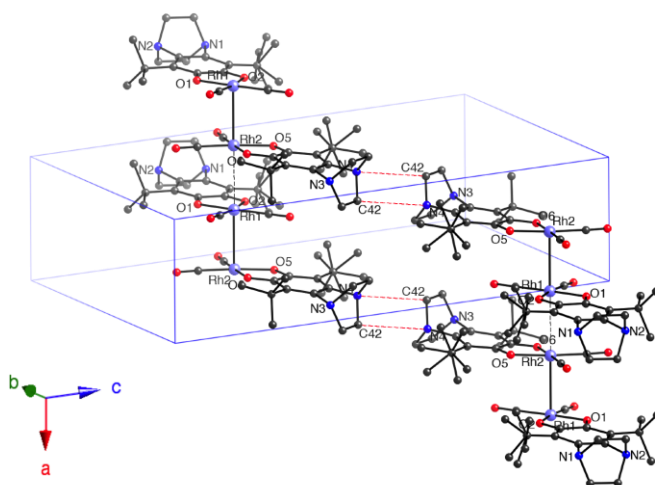


**Figure S7.** Crystal structure of  $[\text{Rh}(3,6\text{-DBSQ-4,5-(}N,N'\text{-DEN))}(\text{CO})_2]_\infty$  (**5**) at 250 K showing the interchain  $\text{C-H}\cdots\text{N}$  hydrogen bonds between adjacent 1D chains;  $\text{N4}\cdots\text{C42} = 3.553(8) \text{ \AA}$ .

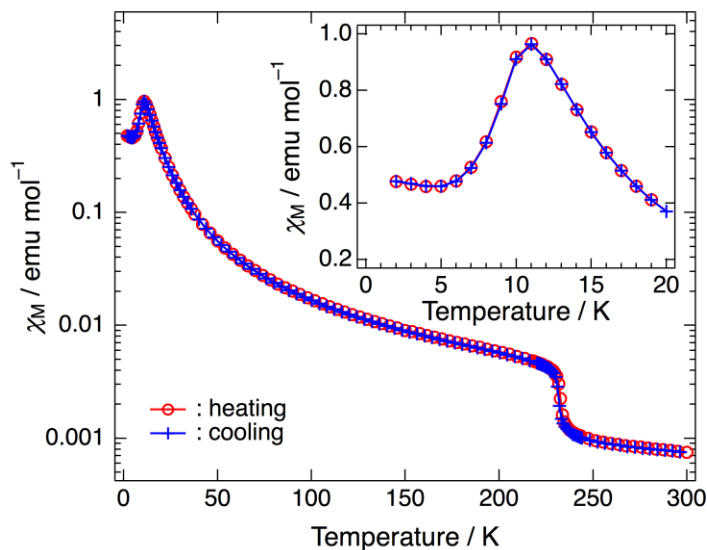


**Figure S8.** Temperature dependence of the molar magnetic susceptibility  $\chi_M$  for  $[\text{Rh}(\text{3,6-DBSQ-4,5-PDO})(\text{CO})_2]_\infty$  (**4**) measured on a polycrystalline sample under an applied magnetic field of 200 Oe. Solid lines are guides for the eye. The insert is an enlarged view of the low temperature region of 2–20 K.

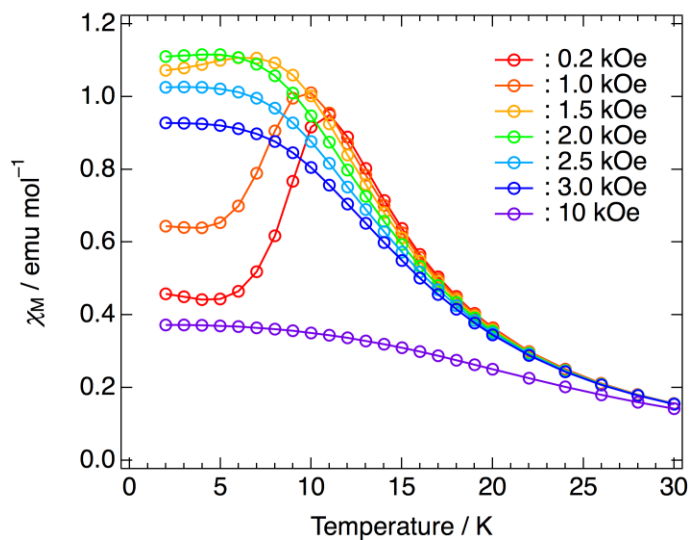


**Figure S9.** Field dependence of  $\chi_M$  vs.  $T$  plots for  $[\text{Rh}(\text{3,6-DBSQ-4,5-PDO})(\text{CO})_2]_\infty$  (**4**) measured on a polycrystalline sample in the temperature region of 2–30 K. Solid lines are guides for the eye.

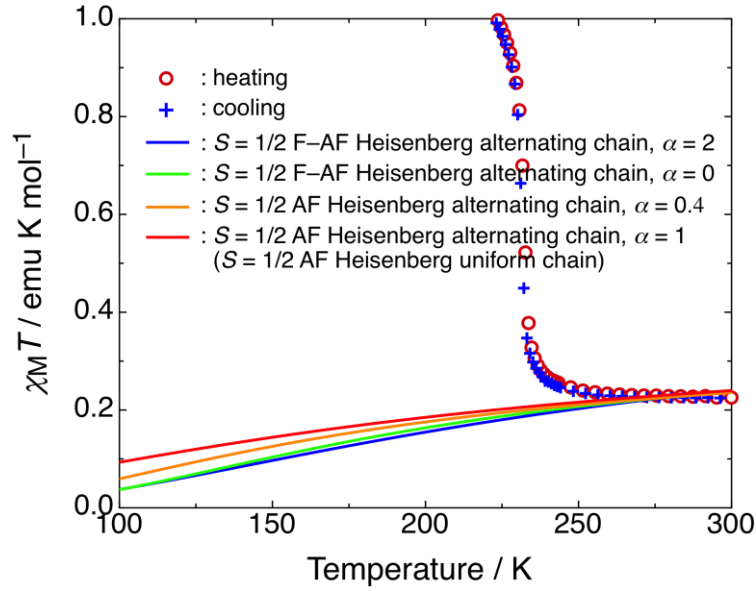


**Figure S10.** Temperature dependence of the product  $\chi_M T$  for  $[\text{Rh}(3,6\text{-DBSQ-4,5-PDO})(\text{CO})_2]_\infty$  (4) in the temperature range of 100–300 K. The red line is the best fit of the RT phase data between 300 and 260 K with the  $S = 1/2$  antiferromagnetic (AF) Heisenberg alternating chain model ( $H = -J \sum [S_{2i} \cdot S_{2i-1} + \alpha S_{2i} \cdot S_{2i+1}]$ ,  $J/k_B = -232(4)$  K with  $\alpha = 1$  ( $S = 1/2$  AF Heisenberg uniform chain model) and  $g = 2.00$ ). For comparison, the best fits to the  $S = 1/2$  AF Heisenberg alternating chain model (orange line,  $J/k_B = -314(5)$  K with  $\alpha = 0.4$  and  $g = 2.00$ ) and the  $S = 1/2$  ferro- and antiferromagnetic (F–AF) Heisenberg alternating chain models ( $H = -\sum [J_1 S_{2i} \cdot S_{2i+1} + J_2 S_{2i} \cdot S_{2i-1}]$  ( $\alpha = J_2/|J_1|$ ): green line,  $J_1/k_B = -493(8)$  K,  $J_2/k_B = +986(16)$  K ( $\alpha = 2$ ) and  $g = 2.00$ ); blue line,  $J_1/k_B = -363(6)$  K,  $J_2/k_B = 0$  K ( $\alpha = 0$ ) and  $g = 2.00$ ) are also shown.



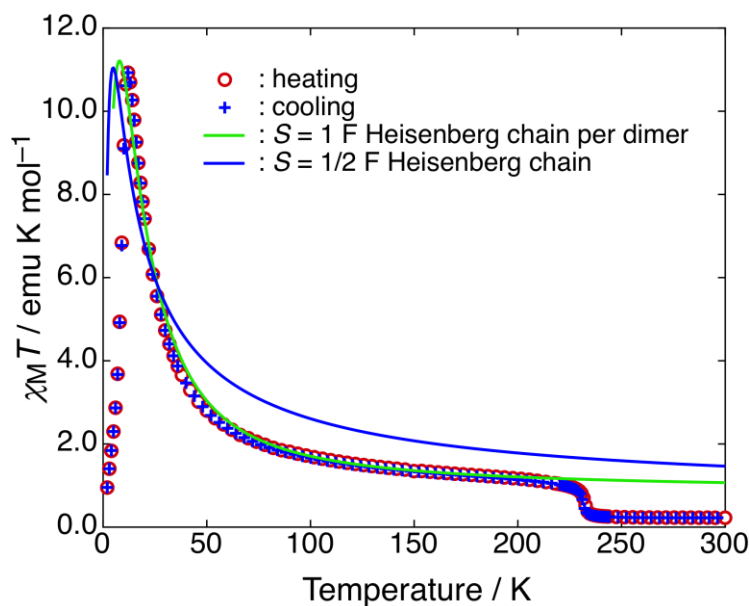


**Figure S11.** Temperature dependence of the product  $\chi_M T$  for  $[\text{Rh}(3,6\text{-DBSQ-4,5-PDO})(\text{CO})_2]_\infty$  (4). The green line is the best fit of the LT phase data between 208 and 10 K with the half-value of the  $S = 1$  ferromagnetic Heisenberg uniform chain model involving the mean-field approximation ( $H = -J \sum S_i \cdot S_{i+1}$ ,  $J/k_B = +56(4)$  K,  $g = 2.59(7)$ , and  $zj'/k_B = -0.45$  K (fixed)). For comparison, the best fit to the  $S = 1/2$  ferromagnetic (F) Heisenberg uniform chain model (Baker equation) with the mean-field approximation (blue line,  $H = -J \sum S_i \cdot S_{i+1}$ ,  $J/k_B = +240$  K,  $g = 2.62$ , and  $zj'/k_B = -0.45$  K (fixed)) is also shown.

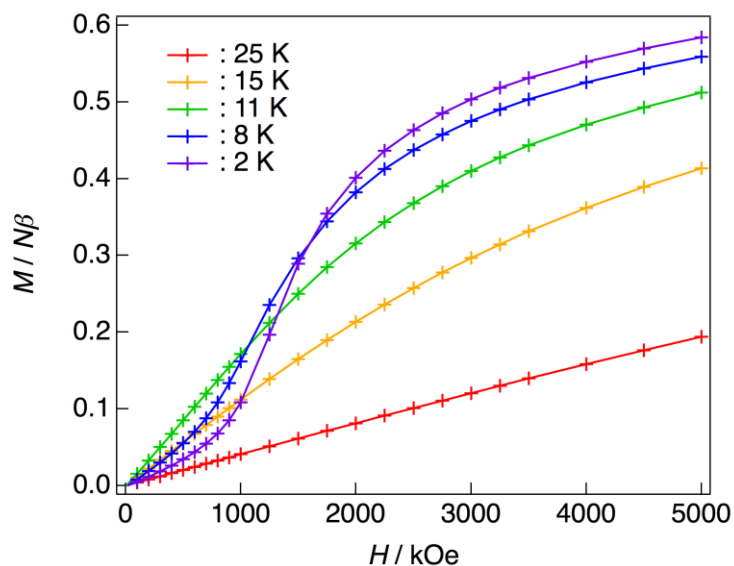


**Figure S12.** Field dependence of magnetization  $M$  for  $[\text{Rh}(3,6\text{-DBSQ-4,5-PDO})(\text{CO})_2]_\infty$  (**4**) measured on a polycrystalline sample at various temperature conditions.

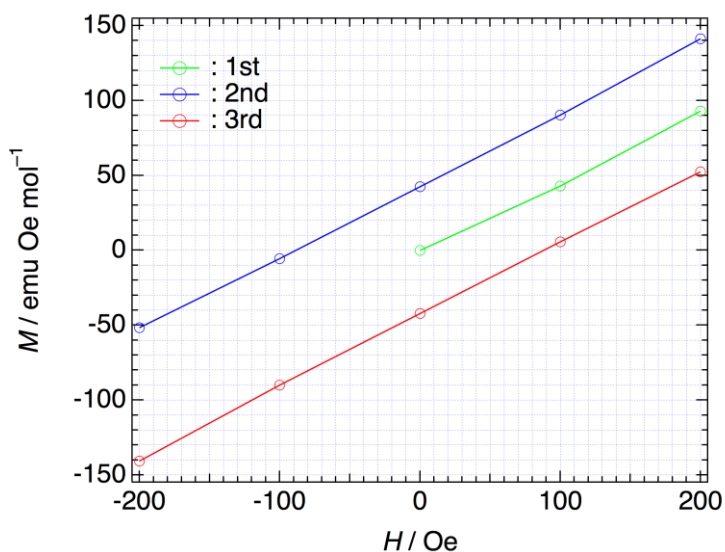


**Figure S13.** Field dependence of magnetization  $M$  between +200 Oe and -200 Oe for  $[\text{Rh}(3,6\text{-DBSQ-4,5-PDO})(\text{CO})_2]_\infty$  (**4**) measured at 2 K on a polycrystalline sample. A very small magnetic hysteresis loop is observed with a coercive field of 88 Oe and remnant magnetization of 42 emu Oe mol<sup>-1</sup> (0.0076  $N\beta$ ). The observed small hysteresis is consistent with the appearance of the out-of-phase signal  $\chi''$  due to the spin canting.